Available online at www.sciencedirect.com
ScienceDirect
Acta Materialia 57 (2009) 980–992
Acta MATERIALIA
www.elsevier.com/locate/actamat

A sintering model for plasma-sprayed zirconia TBCs. Part I: Free-standing coatings

A. Cipitria, I.O. Golosnoy, T.W. Clyne *

Department of Materials Science & Metallurgy, Cambridge University, Pembroke Street, Cambridge CB2 3QZ, UK

Received 9 July 2008; received in revised form 15 October 2008; accepted 15 October 2008
Available online 18 November 2008

Abstract

A sintering model is presented for prediction of changes in the microstructure and dimensions of free-standing, plasma-sprayed (PS) thermal barrier coatings (TBCs). It is based on the variational principle. It incorporates the main microstructural features of PS TBCs and simulates the effects of surface diffusion, grain boundary diffusion and grain growth. The model is validated by comparison with experimental data for shrinkage, surface area reduction and porosity reduction. Predicted microstructural changes are also used as input data for a previously developed thermal conductivity model. Good agreement is observed between prediction and measurement for all these characteristics. The model allows separation of the effects of coating microstructure and material properties, and captures the coupling between densifying and non-densifying mechanisms. A sensitivity analysis is presented, which highlights the importance of the initial pore architecture. Predictions indicate that the microstructural changes which give rise to (undesirable) increases in thermal conductivity and stiffness are very sensitive to surface diffusion.[1]

Keywords: Plasma-sprayed thermal barrier coatings; Modelling; Sintering; Diffusion; Variational principle

1. Introduction

Improvements in the performance of thermal barrier coatings (TBCs) remains a key objective for further development of both land-based and aeroengine gas turbines. In-service degradation, accompanied by increased risk of spallation, is the major concern. There are strong indications [1–8] that spallation is commonly related to sintering and associated stiffening of the zirconia top coat, particularly [9–14] when this is accelerated by the presence of impurities, such as calcia–magnesia–alumina–silica (CMAS), either from the original powder or deposited during service. This concern is likely to become even more prominent as turbine entry temperatures continue to rise. It relates equally to both plasma spray (PS) and physical vapour deposition (PVD) coatings.

The present work is focused on PS TBCs. Their microstructure comprises overlapping splats lying parallel to the substrate, with interlamellar (inter-splat) pores oriented normal to the heat flux direction, through-thickness intra-splat microcracks (created during splat quenching) and globular voids – see Fig. 1. These features confer low through-thickness thermal conductivity ($K \sim 1$ W m^{-1} K^{-1}) and low in-plane stiffness ($E \sim 20$ GPa). The latter is beneficial in reducing the stresses that arise during thermal cycling as a consequence of the mismatch in expansivity between substrate ($\alpha \sim 11$–15×10^{-6} K^{-1}) and coating ($\alpha \sim 9$–11×10^{-6} K^{-1}).

During service, TBCs are exposed to high temperatures for extended periods, leading to sintering. Consequently, increased thermal conductivity [8,15,16] and stiffness [5,7,17–20] have been widely reported. The

* Corresponding author.
E-mail address: twc10@cam.ac.uk (T.W. Clyne).
[1] A compiled version of the sintering model can be downloaded from www.msm.cam.ac.uk/mmc/publications/software.html

1359-6454/$34.00 © 2008 Acta Materialia Inc. Published by Elsevier Ltd. All rights reserved.
doi:10.1016/j.actamat.2008.10.024

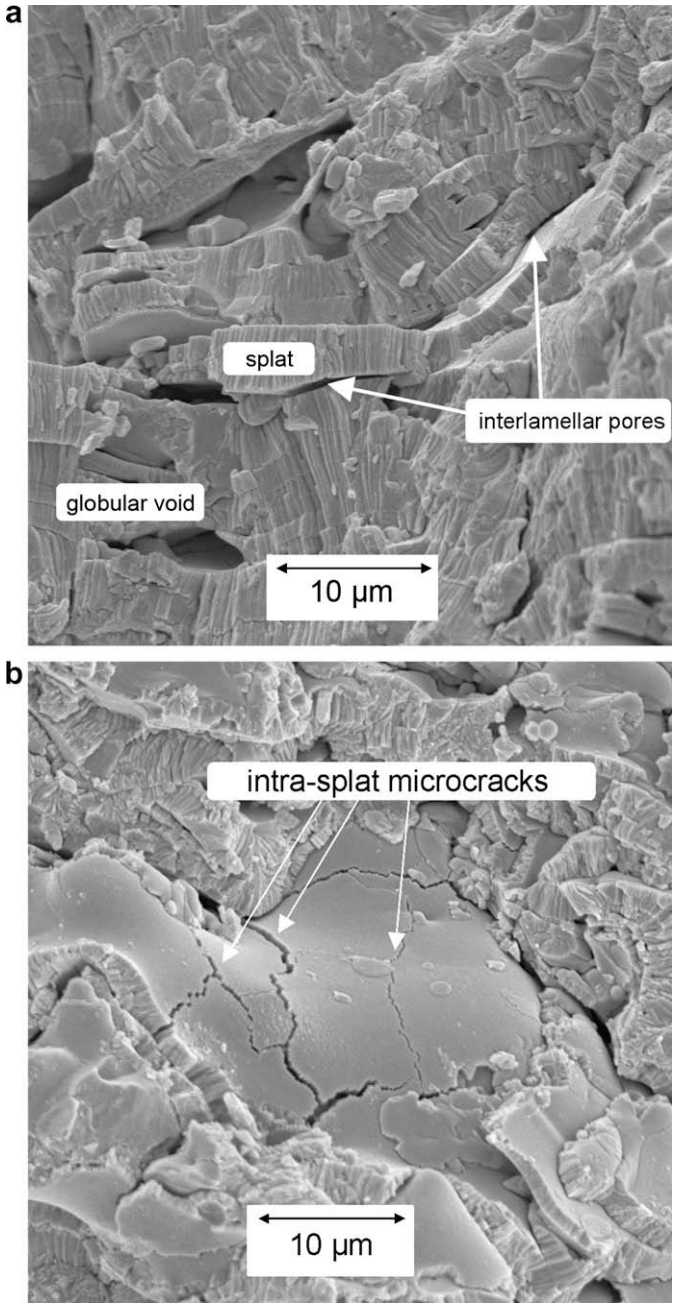

Fig. 1. SEM fracture surfaces of as-sprayed YSZ coatings, from the work of (a) Paul et al. [14] and (b) Tsipas et al. [7].

thermal conductivity rise has been correlated with growth of the inter-splat contact area [21,22], and in-plane stiffening with a combination of inter-splat locking and splat stiffening, due to microcrack healing [19]. There is therefore a strong incentive to obtain improved understanding of how microstructures of this type evolve at high temperature, and how these changes influence the properties and behaviour of the coatings. The sintering model presented here is based on application of the variational principle to diffusional phenomena, which has been broadly described elsewhere [23–26].

2. Framework of the model

2.1. General background

A nomenclature listing is presented as Table 1. Interest is focused on the pore architecture, and the way in which this changes during extended holding at elevated temperature, as a consequence of diffusional processes. The main architectural features of PS TBCs are taken to be inter-splat pores, intra-splat microcracks and globular voids. These are all assumed to be connected to each other, and to the surrounding atmosphere – i.e. there are no occluded pores. Obviously, a number of parameters must be defined, including various dimensions and the volume fraction of each type of porosity, and also certain material properties. Choice of these has been made mostly on the basis of information available in the literature and both the values employed and the sources are listed in tables – see below. The three types of porosity are treated separately, within three superimposed domains. It is assumed that the system evolves in such a way that, during each time step, the change (reduction) in free energy associated with the change in its structure, and the energy dissipated during the diffusional processes involved to effect this change, are such as to optimize the process from an energy point of view. Representative domains are identified, but there is no further spatial discretization within each domain.

Only grain boundary and surface diffusion are treated. Lattice diffusion, diffusion along dislocations, vapour transport and viscous flow of any liquid (vitreous) phases are therefore all neglected. This is thought to be broadly appropriate for these systems, although liquid phase sintering may be significant for cases in which the impurity content is relatively high. It may be noted that, while both grain boundary and surface diffusion will tend to effect changes in pore architecture, and associated reductions in surface area, only grain boundary diffusion causes densification, and hence changes in the macroscopic dimensions of the specimen. In the present version of the model, relating to free-standing coatings, there is no constraint, and hence no stress within the specimen and no creep phenomena. In a companion paper, the effects of attachment to a rigid substrate, leading to stress development and creep, are considered.

2.2. Model geometry

2.2.1. Inter-splat pores

The superscript (1) refers to the inter-splat pore domain, defined in cylindrical coordinates (r, z). A representative volume element is a cylindrical disk of radius r_{s0} and height $2z_{s0}$ (splat thickness), with a cylindrical bridge (contact) of radius r_{b0} (see Fig. 2). (While a cylindrical geometry has been assumed, these volume elements are not intended to represent splats, which are approximately cylindrical, but rather the segments between

Table 1

Nomenclature

Symbols		
a	m	Half-distance between microcrack spacing
A	m^2	Area
b	m	Open dimension of pores or microcracks
D	$m^2\ s^{-1}$	Diffusion coefficient
D_0	$m^2\ s^{-1}$	Pre-exponential factor of the diffusion coefficient
g	m	Grain size
G	$J\ m^{-3}$	Free energy per unit volume of material
h	m	Distance from the centre of a splat to the centre of an inter-splat contact
j	$m^3\ m^{-1}\ s^{-1}$	Volumetric flux per unit length (along an interface)
k_B	$J\ at^{-1}\ K^{-1}$	Boltzmann's constant
L_0	m	Initial half-length of a microcrack
m_m	$m^4\ J^{-1}\ s^{-1}$	Intrinsic grain boundary mobility
M	$m^2\ J^{-1}\ s^{-1}$	Atomic mobility
n	–	No. of modelled unit domains
N_s	–	No. of columnar grains within a representative volume element of a splat
P	–	Porosity
q	$m^3\ m^{-2}\ s^{-1}$	Additional source or sink of material (volumetric flux per unit area)
Q	$J\ mol^{-1}$	Activation energy
r	m	Radius
S	$m^2\ m^{-3}$	Specific surface area
v	$m\ s^{-1}$	Migration velocity of an interface, normal to its surface
V	m^3	Volume of material corresponding to a domain
x	m	Length in x direction
y	m	Length in y direction
z	m	Length in z direction
Greek symbols		
δ	m	Thickness of layer along interface, through which diffusion takes place
γ	$J\ m^{-2}$	Interfacial energy
Π	$J\ s^{-1}\ m^{-3}$	Sum of rates of free energy reduction and energy dissipation, per unit volume of material
Ω	$m^3\ atom^{-1}$	Volume associated with a diffusing species
ξ		Correction factor
Ψ	$J\ s^{-1}\ m^{-3}$	Rate of energy dissipation per unit volume of material
Superscripts		
(1)		Inter-splat pores
(2)		Intra-splat microcracks
(3)		Globular voids
Subscripts		
b		Contact bridge between inter-splat pores or intra-splat microcracks
c		Microcrack
gb		Grain boundary
ip		In-plane
imp		Impurities
m		Grain boundary migration
s		Splat
S		Surface
tt		Through-thickness
t		Total
v		Globular void

microcracks, which are obviously smaller than the splats and do not have a cylindrical geometry.) Inter-splat porosity is represented as the void between these cylindrical disks, with open pore dimension $2(h - z_s)$, where h is the height from the centre of the inter-splat contact to the centre of the splat. The splats contain through-thickness columnar grains, modelled as hexagonal prisms of initial side length g_0. The number of grains within a volume element (splat) is N_s. Fig. 1 shows that columnar grains do not always extend through the complete thickness of a splat and some grain boundaries lie at large angles to the through-thickness (z) direction. The grain structure is therefore represented as both a set of columns and an in-plane boundary extending across the plane of symmetry, at the mid-height of the splat – see Fig. 2. An in-plane grain boundary is also located at the mid-height of the cylindrical bridge, along the inter-splat contact area. The volume of the modelled domain extends over the half-height of the splat, z_{s0}, and the half-height of the pore, $(h - z_s)$.

Microstructural evolution of interlamellar pores is described by the changing values of four independent geometrical parameters: h, z_s, r_s and N_s. The radius of the contact area, r_b, and the grain size, g, can be expressed in terms of these. The independent parameters are associated with the mechanisms of grain boundary diffusion, leading to through-thickness shrinkage (reduction in h), surface diffusion (reduction in z_s), grain boundary diffusion, causing in-plane shrinkage (reduction in r_s), and grain growth (reduction in N_s). As sintering proceeds (Fig. 2, dashed profile), grain boundary diffusion along the columnar grains reduces r_s, causing in-plane shrinkage. Material flows to the in-plane grain boundary, along the inter-splat contact, and to the free surface. Grain boundary diffusion along the inter-splat contact reduces h, resulting in through-thickness shrinkage, and increases r_b. Surface diffusion contributes to pore spheroidization, i.e. reduces z_s, causing the half-height of the pore $(h - z_s)$ to increase, and increases r_b. Finally, grain boundary migration causes an increase in lateral (in-plane) grain size, g, and hence a reduction in N_s (while r_s remains unchanged). Uniform grain growth is assumed (i.e. the migration of individual GBs is not modelled) and N_s decreases continuously.

2.2.2. Intra-splat microcracks

The superscript (2) refers to the intra-splat microcrack domain, defined in Cartesian coordinates (x, y, z). A network of through-thickness microcracks is modelled as two superimposed orthogonal arrays (Fig. 3). The representative volume element for microcracks is a rectangular domain of width $2a_0$ (related to microcrack spacing) and length $2L_0$, with height equal to the splat thickness, $2z_{s0}$. The microcracks, with open dimension $2(a_0 - y_{c0})$, are separated by bridge contacts of width $2x_{b0}$, with a grain boundary along the centre of the contact. The modelled domain thus corresponds to a cuboid of width a_0, length L_0 and height equal to the half-thickness of the splat, z_{s0}. For simplicity, the sintering of only one array is modelled, but the surface area and porosity corresponding to microcracks is doubled, to take account of an orthogonal set, and the in-plane shrinkage is assumed isotropic.

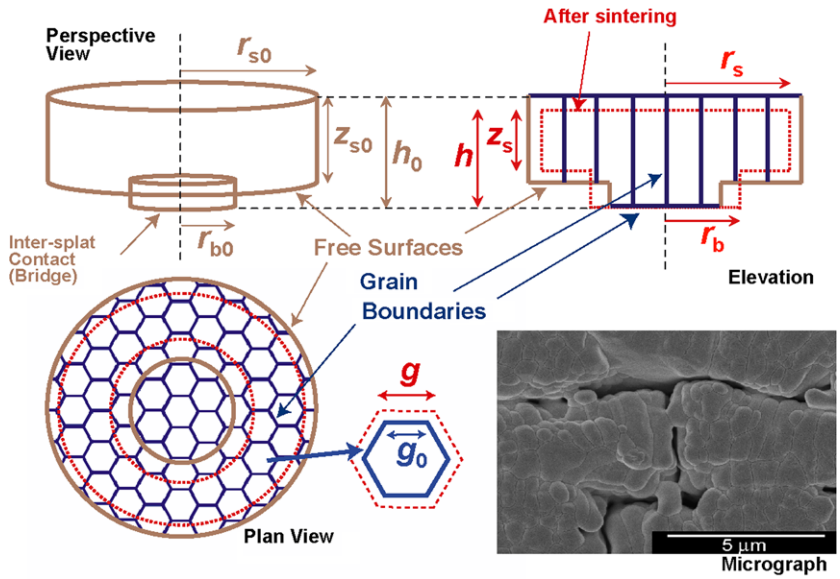

Fig. 2. Schematic depiction of domain (1), representing inter-splat porosity, showing perspective, plan and elevation views of the cylindrical system, an indication of how the shape changes after sintering and an illustrative SEM micrograph (post-heat treatment).

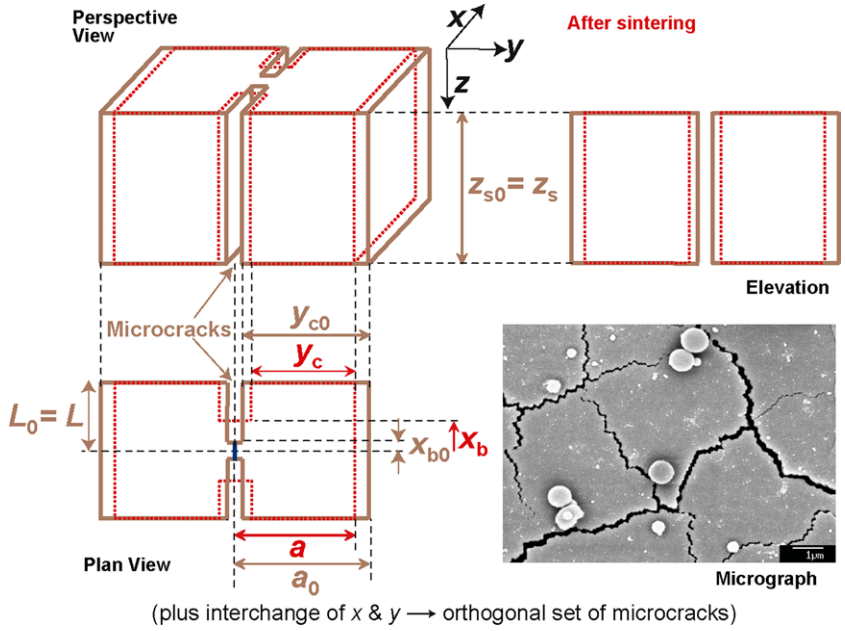

Fig. 3. Schematic depiction of domain (2), representing intra-splat porosity, showing perspective, plan and elevation views, an indication of how the shape changes after sintering and an illustrative SEM micrograph (plan view of a splat).

The microstructural evolution of intra-splat microcracks is described by the changing values of two independent geometrical parameters, a and y_c. The half-width of the intra-splat contact, x_b, is expressed in terms of a and y_c, and the domain length L_0 is assumed constant. The independent parameters are associated with the mechanisms of grain boundary diffusion (reduction in a) and surface diffusion (reduction in y_c). As sintering proceeds (Fig. 3(b), dashed profile), grain boundary diffusion along the intra-splat contact reduces a, resulting in in-plane shrinkage, and increases x_b. Surface diffusion contributes to spheroidization of microcracks, i.e. reduces y_c, which promotes opening of the microcracks ($(a - y_c)$ increases), and increases x_b.

2.2.3. Globular voids

Globular voids, denoted by the superscript (3), are assumed to remain unchanged during sintering, but their contributions to the overall porosity and specific surface area are taken into account. They are modelled as large-scale, spherical pores, with radius r_v – see Fig. 1.

2.3. Formulation of the variational principle

2.3.1. Free energy of the system

The model simulates a free-standing coating, with fully interconnected porosity. Thus, there are no contributions to the free energy from either stored elastic strain energy (since there is no constraint) or pressure acting on free surfaces (since there is no occluded porosity). The only contributions to the free energy per unit volume of material, G, are the surface and grain boundary energies

$$G = \frac{1}{V}\left[\int_{A_S} \gamma_S \mathrm{d}A_S + \int_{A_{gb}} \gamma_{gb}\mathrm{d}A_{gb}\right] \tag{1}$$

where V is the volume of material corresponding to a modelled domain, A_s and A_{gb} are surface and grain boundary areas respectively, and γ_s and γ_{gb} are surface and grain boundary energies. Derivation of the expressions for the free energy of the system is presented in the Appendix (§A.2).

2.3.2. Rate of energy dissipation

The processes that can dissipate energy during microstructural evolution are: (i) diffusion through the lattice; (ii) diffusion along grain boundaries; (iii) diffusion along free surfaces; (iv) grain boundary migration; and (v) creep. Only surface and grain boundary diffusion, together with grain boundary migration, are considered here, and creep does not figure in the current formulation, since the model refers to a free-standing coating, in which no stresses develop. The rate of energy dissipation via these processes (per unit volume of material), Ψ, is given by

$$\Psi = \frac{1}{V}\left[\overbrace{\int_{A_{gb}} \frac{1}{2M_{gb}\Omega\delta_{gb}}(j_{gb})^2\mathrm{d}A_{gb}}^{\text{Grain boundary Diffusion}} + \overbrace{\int_{A_S} \frac{1}{2M_S\Omega\delta_S}(j_S)^2\mathrm{d}A_S}^{\text{Surface diffusion}} + \overbrace{\int_{A_{gb}} \frac{1}{2m_m}(v_m)^2\mathrm{d}A_{gb}}^{\text{Grain boundary migration}}\right] \tag{2}$$

where M is the atomic mobility (see Eq. (3)), Ω is the volume associated with a diffusing species, j is the volumetric flux per unit length (along an interface), δ is the thickness of the layer through which diffusion is taking place, v_m is the grain boundary migration velocity and m_m is the intrinsic grain boundary mobility. The atomic and the intrinsic grain boundary mobilities are taken from Rahaman [27]

$$M = \frac{D_0 \exp(-Q/RT)}{k_B T} \tag{3}$$

$$m_m = \frac{D_{gb0}\exp(-Q_{gb}/RT)}{k_{BT}}\frac{\Omega}{\delta_{gb}} \tag{4}$$

where k_B is the Boltzmann constant. The intrinsic grain boundary mobility can, however, be significantly reduced by the drag force exerted by segregated solutes and second-phase particles (Zener drag). A correction factor ξ_m is applied to account for this effect (see Table 2).

The diffusion fluxes along grain boundaries and free surfaces are assumed to be uniaxial. Matter conservation is satisfied by relating the flux along an interface, j, to its migration velocity, normal to its surface, v, as follows:

$$\nabla j + v = q \tag{5}$$

where ∇ is the divergence operator and q represents additional sources or sinks for material. Derivation of the rate of energy dissipation is presented in the Appendix (§A.3).

2.3.3. Derived equations

The system evolves so as to minimize a function Π, the sum of the rate of free energy reduction, $\dot{G}$, and the energy dissipation rate, Ψ

$$\Pi(\dot{h},\dot{z}_s,\dot{r}_s,\dot{N}_s,\dot{a},\dot{y}_c) = \frac{\mathrm{d}G}{\mathrm{d}t}(\dot{h},\dot{z}_s,\dot{r}_s,\dot{N}_s,\dot{a},\dot{y}_c) + \Psi(\dot{h},\dot{z}_s,\dot{r}_s,\dot{N}_s,\dot{a},\dot{y}_c) \tag{6}$$

The minimum occurs [23–26] at a stationary point of the function Π, so that

$$\delta\Pi = \delta(\dot{G} + \Psi) = 0 \tag{7}$$

This equation represents a set of six ordinary differential equations, which can be written in matrix form – see Eq. (8) below. Expressions for the elements of the matrix, and the vector on the right hand side, are listed in Tables 3 and 4. They depend on the values of the independent variables (h, z_s, r_s, N_s, a,y_c), but not on their rates of change ($\dot{h},\dot{z}_s,\dot{r}_s,\dot{N}_s,\dot{a},\dot{y}_c$). The matrix is symmetric and non-singular, so it can be inverted algebraically. The set of equations is solved numerically after each time step, using the fourth-order Runge–Kutta method

Table 2
Material property input data for the model.

Property	Units	Value	Source
D_{s0}	$m^2\ s^{-1}$	1.0×10^{-3}	See [38]
Q_s	$J\ mol^{-1}$	3.14×10^5	See [38]
D_{gb0}	$m^2\ s^{-1}$	1.0×10^{-3}	[39]
Q_{gb}	$J\ mol^{-1}$	3.70×10^5	[39]
ξ_{imp} [a]		20	See [38]
ξ_m [b]		1.00×10^{-4}	See [38]
γ_s	$J\ m^{-2}$	0.30	[40]
γ_{gb}	$J\ m^{-2}$	0.15	[41]
Ω	m^3	3.374×10^{-29}	See [38]
δ_s	m	3.231×10^{-10}	See [38]
δ_{gb}	m	6.462×10^{-10}	See [38]

[a] D_{s0} and D_{gb0} are increased by a correction factor, ξ_{imp}, in order to account for the increase in sintering rate due to segregation of impurities to free surfaces and grain boundaries.

[b] The intrinsic grain boundary mobility, m_m, is decreased by a correction factor, ξ_m, in order to account for the drag force exerted by segregated solutes (solute drag) and by second-phase particles (Zener drag).

Table 3
Elements of the matrix for the differential equations related to interlamellar pores.

$$\frac{\partial\left(\frac{dG_\lambda^{(1)}}{dt}\right)}{\partial \dot{h}} = \frac{1}{V^{(1)}} C_1^{(1)}$$
$$\frac{\partial\left(\frac{dG_\lambda^{(1)}}{dt}\right)}{\partial \dot{z}_s} = \frac{1}{V^{(1)}} C_2^{(1)}$$
$$\frac{\partial\left(\frac{dG_\lambda^{(1)}}{dt}\right)}{\partial \dot{r}_s} = \frac{1}{V^{(1)}} C_3^{(1)}$$
$$\frac{\partial\left(\frac{dG_\lambda^{(1)}}{dt}\right)}{\partial \dot{N}_s} = \frac{1}{V^{(1)}} C_4^{(1)}$$

$$C_1^{(1)} = \gamma_S \pi r_b \left(1 + \frac{r_b}{h - z_s}\right) - \gamma_{gb} \frac{\pi}{2} \frac{r_b^2}{h - z_s}$$
$$C_2^{(1)} = \gamma_S \pi \left((r_s^2 - r_b^2)\left(\frac{1}{h - z_s} - \frac{1}{r_b}\right) - 2r_b\right) + \gamma_{gb} \frac{\pi}{2} \frac{(r_b^2 - r_s^2)}{h - z_s}$$
$$C_3^{(1)} = \gamma_S 2\pi r_s \left(1 + \frac{z_s}{h - z_s} - \frac{z_s}{r_b}\right) +$$
$$\gamma_{gb}\left(\pi r_s - \frac{\pi r_s z_s}{h - z_s} - \sqrt{2\sqrt{3}\pi N_s} \frac{1}{r_s^2}\left(r_{b0}^2 (h_0 - z_{s0}) + r_{s0}^2 z_{s0}\right)\right)$$
$$C_4^{(1)} = \gamma_{gb} \frac{\sqrt{3}\pi}{\sqrt{2\sqrt{3}\pi N_s}} \frac{(r_{b0}^2 (h_0 - z_{s0}) + r_{s0}^2 z_{s0})}{r_s}$$

After full densification :

$$C_1^{(1)} = 0$$
$$C_2^{(1)} = 0$$
$$C_3^{(1)} = \gamma_{gb}\left(2\pi r_s - \sqrt{2\sqrt{3}\pi N_s} \frac{1}{r_s^2}\left(r_{b0}^2 (h_0 - z_{s0}) + r_{s0}^2 z_{s0}\right)\right)$$
$$C_4^{(1)} = \gamma_{gb} \frac{\sqrt{3}\pi}{\sqrt{2\sqrt{3}\pi N_s}} \frac{(r_{b0}^2 (h_0 - z_{s0}) + r_{s0}^2 z_{s0})}{r_s}$$

$$\frac{\partial^2 \Psi^{(1)}}{(\partial \dot{h})^2} = \frac{1}{V^{(1)}}\left(2C_6^{(1)} + \frac{1}{6} C_8^{(1)} (h - z_s) r_b^2\right)$$
$$\frac{\partial^2 \Psi^{(1)}}{\partial \dot{h} \partial \dot{z}_s} = -\frac{1}{V^{(1)}} \frac{1}{12} C_8^{(1)} (h - z_s)(r_s^2 - r_b^2)$$
$$\frac{\partial^2 \Psi^{(1)}}{\partial \dot{h} \partial \dot{r}_s} = \frac{1}{V^{(1)}}\left[4C_6^{(1)} \frac{h}{r_s} + C_8^{(1)}\left(-\frac{1}{2}\frac{(h - z_s) z_s}{r_s}(r_s^2 - r_b^2) + \frac{1}{3}\frac{(h - z_s)}{r_s}\left(r_b^2 (h - z_s) + r_s^2 z_s\right)\right)\right]$$
$$\frac{\partial^2 \Psi^{(1)}}{(\partial \dot{z}_s)^2} = \frac{1}{V^{(1)}}\left[2C_7^{(1)} + \frac{1}{6} C_8^{(1)} \frac{(h - z_s)}{r_b^2}(r_s^2 - r_b^2)^2\right]$$
$$\frac{\partial^2 \Psi^{(1)}}{\partial \dot{z}_s \partial \dot{r}_s} = \frac{1}{V^{(1)}}\left[4C_7^{(1)} \frac{z_s}{r_s} + C_8^{(1)}\left(\frac{1}{2}\frac{(h - z_s) z_s}{r_s r_b^2}(r_s^2 - r_b^2)^2\right) -\right.$$
$$\left. -C_8^{(1)}\left(\frac{1}{6}\frac{(h - z_s)}{r_b^2 r_s}(r_s^2 - r_b^2)\left(r_b^2 (h - z_s) + r_s^2 z_s\right)\right)\right]$$
$$\frac{\partial^2 \Psi^{(1)}}{(\partial \dot{r}_s)^2} = \frac{1}{V^{(1)}}\left[8C_7^{(1)} \frac{z_s^2}{r_s^2} + 8C_6^{(1)} \frac{h^2}{r_s^2} + 2C_5^{(1)} +\right.$$
$$\left. +2C_8^{(1)} \frac{(h - z_s)}{r_b^2 r_s^2}\left(z_s^2 (r_s^2 - r_b^2)^2 - z_s (r_s^2 - r_b^2)\left(r_b^2 (h - z_s) + r_s^2 z_s\right) + \frac{1}{3}\left(r_b^2 (h - z_s) + r_s^2 z_s\right)^2\right)\right]$$
$$\frac{\partial^2 \Psi^{(1)}}{(\partial \dot{N}_s)^2} = \frac{2C_9^{(1)}}{V^{(1)}}$$

$$C_5^{(1)} = \frac{\pi}{3M_{gb}\Omega\delta_{gb}} \sqrt{\frac{2\pi}{\sqrt{3}N_s}} \frac{1}{r_s}\left(r_b^2 h^3 + (r_s^2 - r_b^2) z_s^3\right)$$
$$C_6^{(1)} = \frac{\pi}{16M_{gb}\Omega(\delta_{gb}/2)} r_b^4$$
$$C_7^{(1)} = \frac{\pi}{4M_S\Omega\delta_S}\left(r_s^4 \ln\frac{r_s}{r_b} - r_s^2 (r_s^2 - r_b^2) + \frac{r_s^4 - r_b^4}{4}\right)$$
$$C_8^{(1)} = \frac{\pi r_b}{M_S\Omega\delta_S}$$
$$C_9^{(1)} = \frac{\pi}{8}\sqrt{\frac{\pi N_s}{2\sqrt{3}}} \frac{\delta_{gb}}{M_{gb}\xi_m\Omega} \frac{r_s (r_{b0}^2 (h_0 - z_{s0}) + r_{s0}^2 z_{s0})}{N_s^3}$$

After full densification :

$$C_5^{(1)} = \frac{\pi}{3M_{gb}\Omega\delta_{gb}} \sqrt{\frac{2\pi}{\sqrt{3}N_s}} \frac{1}{r_s} r_s^2 h^3$$
$$C_6^{(1)} = \frac{\pi}{16M_{gb}\Omega(\delta_{gb}/2)} r_s^4$$
$$C_7^{(1)} = 0$$
$$C_8^{(1)} = 0$$
$$C_9^{(1)} = \frac{\pi}{8}\sqrt{\frac{\pi N_s}{2\sqrt{3}}} \frac{\delta_{gb}}{M_{gb}\xi_m\Omega} \frac{r_s (r_{b0}^2 (h_0 - z_{s0}) + r_{s0}^2 z_{s0})}{N_s^3}$$

$$\begin{pmatrix} \frac{\partial^2 \Psi^{(1)}}{(\partial \dot{h})^2} & \frac{\partial^2 \Psi^{(1)}}{\partial \dot{h} \partial \dot{z}_s} & \frac{\partial^2 \Psi^{(1)}}{\partial \dot{h} \partial \dot{r}_s} & 0 & 0 & 0 \\ \frac{\partial^2 \Psi^{(1)}}{\partial \dot{h} \partial \dot{z}_s} & \frac{\partial^2 \Psi^{(1)}}{(\partial \dot{z}_s)^2} & \frac{\partial^2 \Psi^{(1)}}{\partial \dot{z}_s \partial \dot{r}_s} & 0 & 0 & 0 \\ \frac{\partial^2 \Psi^{(1)}}{\partial \dot{h} \partial \dot{r}_s} & \frac{\partial^2 \Psi^{(1)}}{\partial \dot{z}_s \partial \dot{r}_s} & \frac{\partial^2 \Psi^{(1)}}{(\partial \dot{r}_s)^2} & 0 & 0 & 0 \\ 0 & 0 & 0 & \frac{\partial^2 \Psi^{(1)}}{(\partial \dot{N}_s)^2} & 0 & 0 \\ 0 & 0 & 0 & 0 & \frac{\partial^2 \Psi^{(2)}}{(\partial \dot{a})^2} & \frac{\partial^2 \Psi^{(2)}}{\partial \dot{a} \partial \dot{y}_c} \\ 0 & 0 & 0 & 0 & \frac{\partial^2 \Psi^{(2)}}{\partial \dot{a} \partial \dot{y}_c} & \frac{\partial^2 \Psi^{(2)}}{(\partial \dot{y}_c)^2} \end{pmatrix} \begin{pmatrix} \dot{h} \\ \dot{z}_s \\ \dot{r}_s \\ \dot{N}_s \\ \dot{a} \\ \dot{y}_c \end{pmatrix}$$
$$= -\begin{pmatrix} \frac{\partial\left(\frac{dG^{(1)}}{dt}\right)}{\partial \dot{h}} \\ \frac{\partial\left(\frac{dG^{(1)}}{dt}\right)}{\partial \dot{z}_s} \\ \frac{\partial\left(\frac{dG^{(1)}}{dt}\right)}{\partial \dot{r}_s} \\ \frac{\partial\left(\frac{dG^{(1)}}{dt}\right)}{\partial \dot{N}_s} \\ \frac{\partial\left(\frac{dG^{(2)}}{dt}\right)}{\partial \dot{a}} \\ \frac{\partial\left(\frac{dG^{(2)}}{dt}\right)}{\partial \dot{y}_c} \end{pmatrix} \quad (8)$$

Table 4
Elements of the matrix for the differential equations related to intra-splat microcracks.

$$\frac{\partial\left(\frac{dG_\lambda^{(2)}}{dt}\right)}{\partial \dot{a}} = \frac{1}{V^{(2)}} C_1^{(2)}$$
$$\frac{\partial\left(\frac{dG_\lambda^{(2)}}{dt}\right)}{\partial \dot{y}_c} = \frac{1}{V^{(2)}} C_2^{(2)}$$
$$\frac{\partial^2 \Psi^{(2)}}{(\partial \dot{a})^2} = \frac{1}{V^{(2)}} 2\left(C_3^{(2)} + C_6^{(2)}\right)$$
$$\frac{\partial^2 \Psi^{(2)}}{\partial \dot{a} \partial \dot{y}_c} = \frac{1}{V^{(2)}} C_5^{(2)}$$
$$\frac{\partial^2 \Psi^{(2)}}{(\partial \dot{y}_c)^2} = \frac{1}{V^{(2)}} 2C_4^{(2)}$$

$$C_1^{(2)} = \gamma_S z_{s0}\left(\frac{x_b}{a - y_c} + 1\right) - \gamma_{gb} \frac{z_{s0}}{2} \frac{x_b}{a - y_c}$$
$$C_2^{(2)} = \gamma_S z_{s0}\left(\frac{L_0 - x_b}{a - y_c} - 1\right) - \gamma_{gb} \frac{z_{s0}}{2}\left(\frac{L_0 - x_b}{a - y_c}\right)$$
$$C_3^{(2)} = \frac{1}{6M_S\Omega\delta_S} z_{s0} (a - y_c) x_b^2$$
$$C_4^{(2)} = \frac{1}{6M_S\Omega\delta_S} z_{s0} (a - y_c)(L_0 - x_b)^2\left(1 + \frac{L_0 - x_b}{a - y_c}\right)$$
$$C_5^{(2)} = -\frac{1}{6M_S\Omega\delta_S} z_{s0} (a - y_c) x_b (L_0 - x_b)$$
$$C_6^{(2)} = \frac{1}{6M_{gb}\Omega_2^1\delta_{gb}} z_{s0} x_b^3$$

3. Model predictions and comparisons with experiment

The input data for pore geometry and material properties are summarized in Tables 2 and 5. The validity of the model is explored through comparisons with experiments, performed on free-standing, plasma-sprayed YSZ coatings (AE1 in the notation of a previous publication [14]).

Table 5
Pore architecture input data for the model.

Property	Units	Monosized distance	Bimodal distance		(0.5 r_s,0.5 r_b)	(2 r_s, 2 r_b)	Source
Inter-splat pores							
z_{s0}	m	1.25×10^{-6}	1.25×10^{-6}	$1.25\ 10^{-6}$	1.25×10^{-6}	1.25×10^{-6}	Fig. 1(a)
h_0	m	1.313×10^{-6}	1.275×10^{-6}	$1.350\ 10^{-6}$	1.313×10^{-6}	1.313×10^{-6}	f(z_{s0},b_0)
r_{s0}	m	3.00×10^{-6}	3.00×10^{-6}	$3.00\ 10^{-6}$	1.50×10^{-6}	6.00×10^{-6}	f((A_b/A_T)$_0$)
r_{b0}	m	1.162×10^{-6}	1.162×10^{-6}	$1.162\ 10^{-6}$	5.809×10^{-7}	2.324×10^{-6}	f((A_b/A_T)$_0$)
g_0	m	5.00×10^{-7}	5.00×10^{-7}	$5.00\ 10^{-7}$	5.00×10^{-7}	5.00×10^{-7}	Fig. 2
b_0=2(h_0-z_{s0})	m	$125\ 10^{-9}$	50×10^{-9}	200×10^{-9}	125×10^{-9}	$125\ 10^{-9}$	[3,14,18,28,34]
(h-z_s)$^{-1}$	m^{-1}	1.6×10^7	4.0×10^7	1.0×10^7	1.6×10^7	1.6×10^7	
(A_b/A_T)$_0$ $\propto$ (r_{b0}/r_{s0})^2	%	15	15	15	15	15	[35]
P	%	4.05	1.67	6.30	4.05	4.05	[36,37]
S	$m^2\ m^{-3}$	6.88×10^5	6.83×10^5	$6.92\ 10^5$	7.01×10^5	6.81×10^5	[36]
Intra-splat microcracks							
a_0	m	3.75×10^{-6}	3.75×10^{-6}	$3.75\ 10^{-6}$	3.75×10^{-6}	3.75×10^{-6}	Fig. 1(b), Fig. 3
y_{c0}	m	3.688×10^{-6}	3.725×10^{-6}	$3.650\ 10^{-6}$	3.688×10^{-6}	3.688×10^{-6}	f(a_0,b_0)
x_{b0}	m	1.125×10^{-6}	1.125×10^{-6}	$1.125\ 10^{-6}$	1.125×10^{-6}	1.125×10^{-6}	f((A_b/A_T)$_0$)
L_0	m	3.75×10^{-6}	3.75×10^{-6}	$3.75\ 10^{-6}$	3.75×10^{-6}	3.75×10^{-6}	Fig. 1(b), Fig. 3
b_0=2(a_0-y_{c0})	m	$125\ 10^{-9}$	50×10^{-9}	200×10^{-9}	125×10^{-9}	$125\ 10^{-9}$	[3,14,18,28,34]
(a-y_c)$^{-1}$	m^{-1}	1.6×10^7	4.0×10^7	1.0×10^7	1.6×10^7	1.6×10^7	
(A_b/A_T)$_0$ $\propto$ (x_{b0}/ L_0)	%	30	30	30	30	30	
P	%	2 (1.17)	2 (0.47)	2 (1.87)	2 (1.17)	2 (1.17)	[36,37]
S	$m^2\ m^{-3}$	2 (1.93×10^5)	2 (1.89×10^5)	2 (1.98×10^5)	2 (1.93×10^5)	2 (1.93×10^5)	[36]
Globular voids							
r_v	m	1.00×10^{-6}	1.00×10^{-6}	$1.00\ 10^{-6}$	1.00×10^{-6}	1.00×10^{-6}	[35,36]
P	%	4	4	4	4	4	[36,37]
S	m^2m^{-3}	1.25×10^5	1.25×10^5	$1.25\ 10^5$	1.25×10^5	1.25×10^5	[36]
Total							
P	%	10.4	6.6	14.0	10.4	10.4	[28,35–37]
S	m^2m^{-3}	1.20×10^6	1.19×10^6	$1.21\ 10^6$	1.21×10^6	1.19×10^6	[14,36]

3.1. Coating shrinkage

The model gives predictions for coating shrinkage, in both through-thickness and in-plane directions. Through-thickness shrinkage is caused by sintering of inter-splat pores (Eq. (9)), whereas in-plane shrinkage arises from sintering of both inter-splat pores and intra-splat microcracks (Eq. (10)): it is isotropic in-plane (see §A.1.1):

$$\left(\frac{\Delta L}{L_0}\right)_{tt} = -\frac{h-h_0}{h_0} \tag{9}$$

$$\left(\frac{\Delta L}{L_0}\right)_{ip} = -\frac{r_s-r_{s0}}{r_{s0}} - \frac{a-a_0}{a_0} \tag{10}$$

Fig. 4 compares previously reported dilatometry data [14] with model predictions for coating shrinkage, in through-thickness and in-plane directions, at 1200 and 1400°C. The predictions are based on a bimodal distribution of inter-splat pores and intra-splat microcracks, with open dimension 50 and 200 nm. Predictions for a monosized distribution (125 nm) of pores and microcracks have not been included, due to its similarity to those for a bimodal distribution (in the plotted timeframe). It can be seen that experimental and predicted curves exhibit good agreement, both in terms of the absolute values and the general trends. There are some minor discrepancies, but these are attributable to either experimental artefacts or the simplifications incorporated in the model.

3.2. Surface area reduction

The contributions to the surface area of inter-splat pores, intra-splat microcracks and globular voids, and their reduction during sintering, can be predicted. The surface area per unit volume of material (including pores), S, is given (see §A.1.2) by

$$S = S^{(1)} + 2S^{(2)} + S^{(3)} \tag{11}$$

in which the factor of 2 reflects the presence of two orthogonal sets of microcracks. Fig. 5(a) compares previously reported experimental (BET) surface area data [14] with model predictions, for monosized (125 nm) and bimodal (50 and 200 nm) distributions of inter-splat pores and intra-splat microcracks, at 1400 °C. Experimental data points represent the average of three measurements (performed on three different samples) for as-sprayed coatings, the average of two measurements for 1 h heat-treated coatings and just one measurement for the 10 h heat treatment. The variability for the multi-measurement cases was so small that error bars would not be visible on the scale of this plot. While the experimental data are clearly limited, good agreement is again observed, particularly for the bimodal pore size distribution. A bimodal pore size distribution leads to a two-stage surface area reduction, with a fast initial decrease, associated with the finer pores and microcracks, followed by a slower reduction, associated with coarser pores and microcracks.

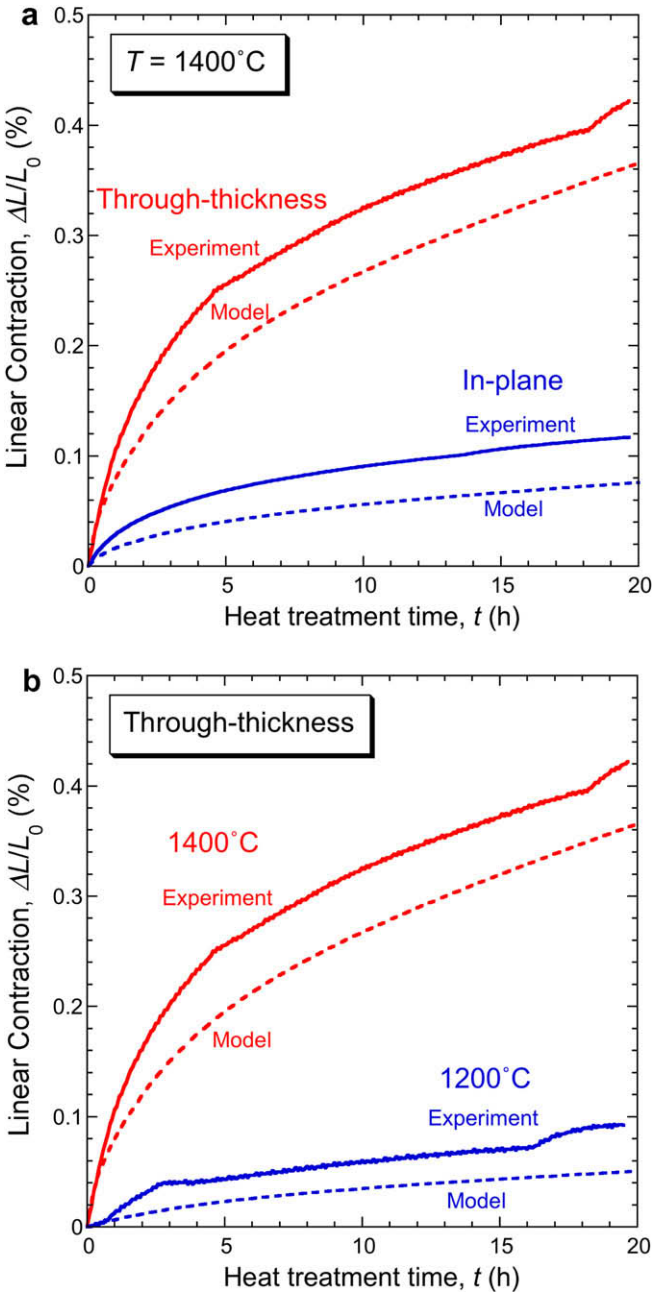

Fig. 4. Comparison between experimental data [14] and model predictions for coating shrinkage, (a) at 1400 °C in both through-thickness and in-plane directions and (b) in the through-thickness direction, at both 1200 and 1400 °C. The model predictions are based on a bimodal distribution (50 and 200 nm) for the initial open dimension of both inter-splat pores and microcracks.

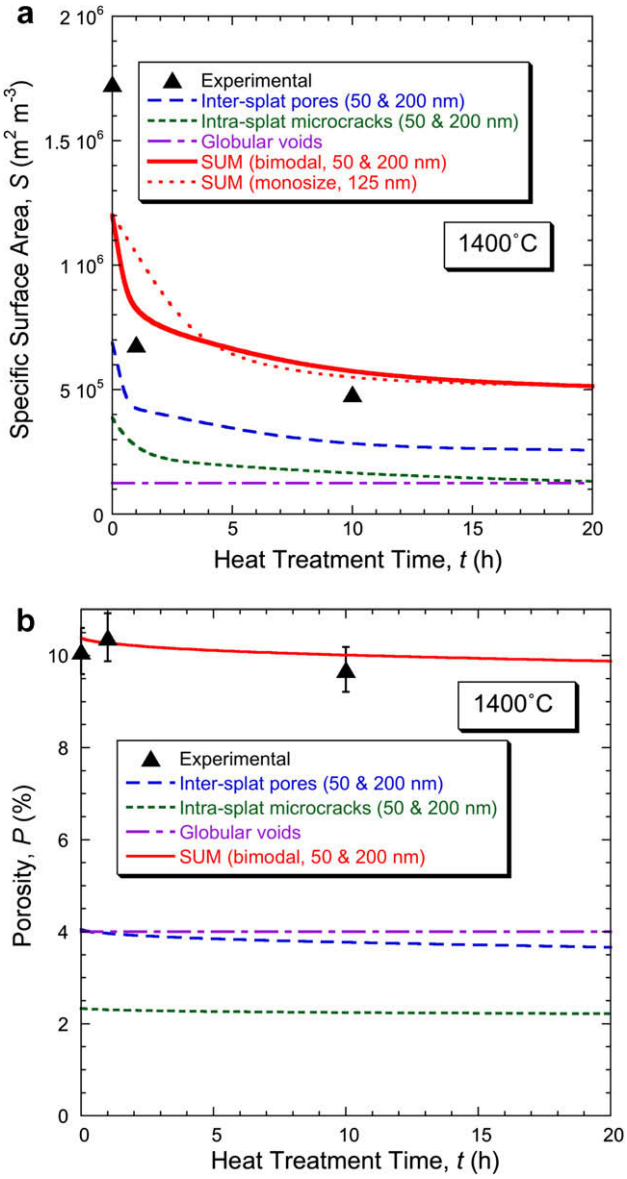

Fig. 5. Comparison between experimental data [14] and model predictions for (a) surface area reduction and (b) porosity, at 1400 °C.

3.3. Porosity reduction

The changing contributions to the overall porosity of inter-splat pores, intra-splat microcracks and globular voids can also be predicted:

$$P = P^{(1)} + 2P^{(2)} + P^{(3)} \tag{12}$$

Fig. 5(b) compares experimental porosity data [28], obtained using mercury intrusion porosimetry, with model predictions, for a bimodal distribution (50 and 200 nm) of inter-splat pores and intra-splat microcracks, at 1400 °C. (The predictions for a monosized distribution have not been included, due to its similarity to those for a bimodal distribution.) Again, the experimental data are limited (and changes tend to be small relative to the scatter), but the predicted behaviour is certainly consistent with observations.

3.4. Effect of microstructural evolution on thermal conductivity

The same geometrical representation of inter-splat porosity has been previously employed to predict through-thickness thermal conductivity [22]. Fig. 6(a) shows predictions for the growth of inter-splat fractional contact area, for monosized (125 nm) and bimodal (50 and 200 nm) pore size distributions. Fig. 6(b) compares

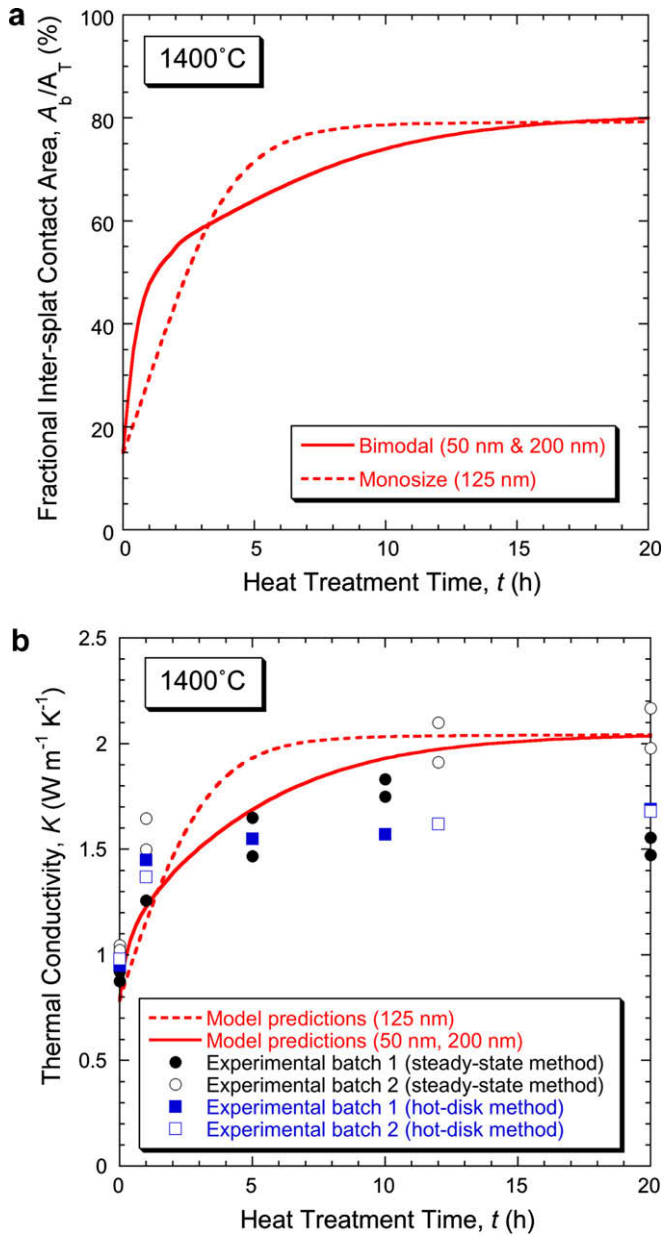

Fig. 6. (a) Predicted evolution at 1400 °C of the fractional inter-splat contact area growth and (b) comparison between experimental thermal conductivity data [14,28] and predictions obtained using the "two flux regimes" model [22], based on the inter-splat contact area predictions shown here.

experimental thermal conductivity data [14,28], measured using the hot disk [29] and steady-state bi-substrate [30] methods, with predictions from the thermal conductivity model, using evolving microstructural parameters obtained from the sintering model. Again, there is good general agreement, although there is inevitably significant scatter in the experimental data. In a similar way to the surface area reduction kinetics, the growth of inter-splat contact area differs for monosized and bimodal pore size distributions. This suggests that surface diffusion contributes strongly to microstructural changes which affect coating properties. It may be noted that neither the sintering model nor the thermal conductivity model incorporate any arbitrarily adjustable parameters.

4. Sensitivity analysis

4.1. Sensitivity to initial pore geometry

As expected, the rate at which the microstructure evolves is sensitive to the scale of the structure. For example, Fig. 7 shows how reductions or increases in the size of inter-splat contact bridges (r_b) and the spacing between them (r_s), for a given fractional contact area (A_b/A_T), affect both shrinkage and inter-splat area growth. This is clearly a

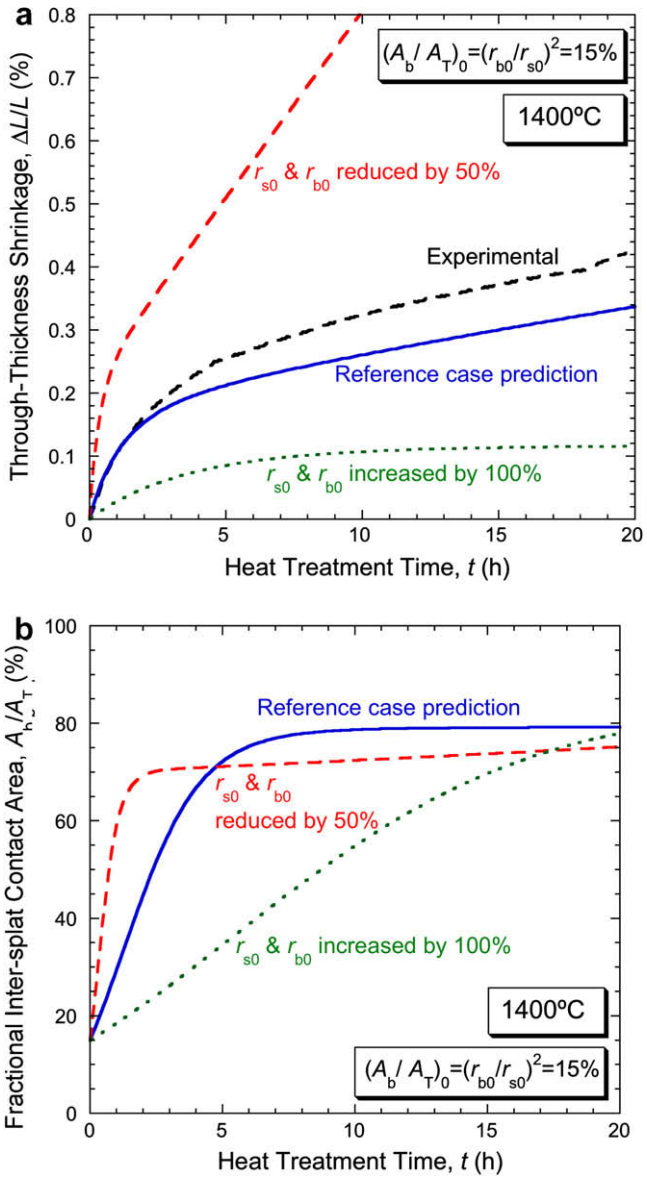

Fig. 7. Predicted sensitivity of (a) through-thickness shrinkage rate and (b) fractional inter-splat contact area growth, to variations in the size and separation of inter-splat contacts, for a temperature of 1400 °C and an initial fractional contact area of 15%.

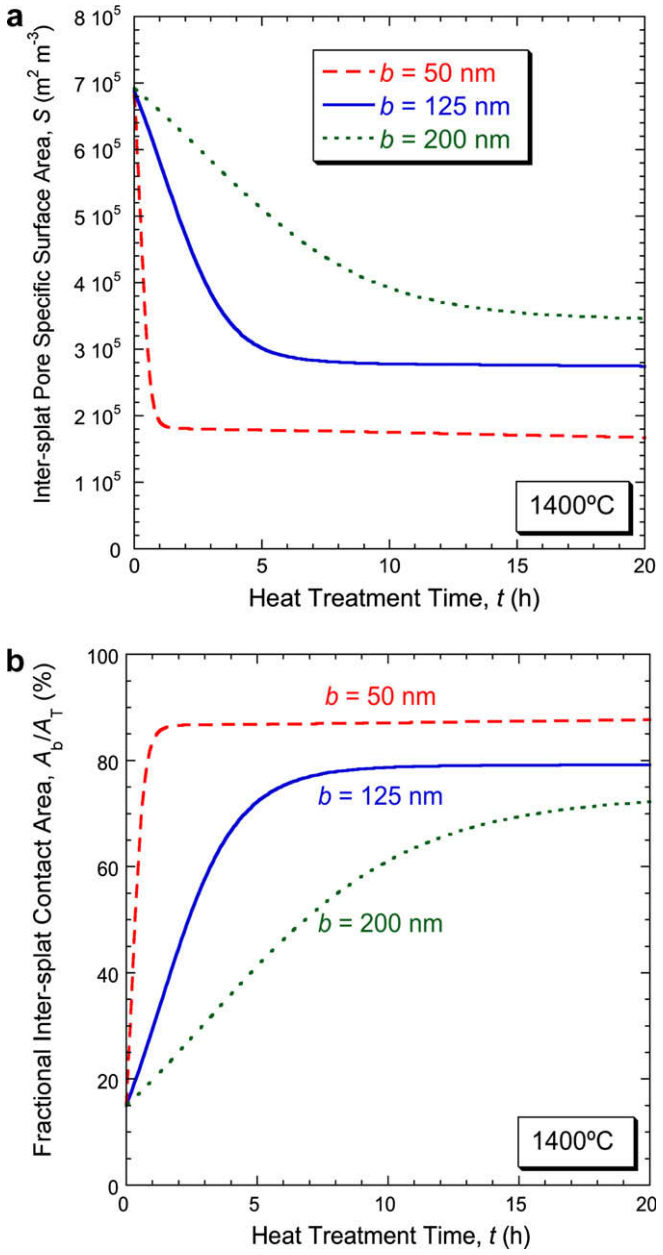

Fig. 8. Predicted sensitivity of inter-splat pore (a) specific surface area and (b) fractional contact area growth, to the initial open pore dimension, for a temperature of 1400 °C.

consequence of changes in the diffusion distances associated with sintering.

Fig. 8 illustrates the effect of variations in the initial open pore dimension, b, on the evolution of the surface area and the inter-splat contact area. Predictions are given for three values (50, 125 and 200 nm). These cases have similar surface areas, but different curvature gradients (the reciprocal of the half-open dimension is taken as the effective curvature), which is the basic driving force for surface diffusion. It can be seen that finer pores lead to faster spherodization – i.e. more rapid surface area reduction and contact area growth. The same trend is observed on changing the initial open dimension of intra-splat microcracks.

4.2. Sensitivity to diffusivities

Sintering is sensitive to the values of the surface and grain boundary diffusivities. Surface diffusion is a non-densifying process, which redistributes material around the free (pore) surfaces and reduces the surface area, without causing shrinkage. Grain boundary diffusion, on the other hand, is a densifying mechanism, which moves material from the interior to the surface and reduces both the pore surface area and the pore volume. Fig. 9 shows predicted effects of raising these diffusivities on through-thickness shrinkage rates, surface area reduction and inter-splat contact area, for a bimodal distribution of pores and microcracks (50 and 200 nm).

It can be seen in Fig. 9(a) that increasing D_{gb0} accelerates the shrinkage, as expected. However, an increase in D_{s0} actually reduces the shrinkage rate, rather than having no effect, as might have been expected. This is due to more of the driving force for diffusion (effectively the presence of sharp gradients of curvature) being consumed by surface diffusion (which causes no shrinkage) and hence being unavailable to promote grain boundary diffusion – i.e. the two processes are in competition with each other. This is in agreement with predictions from previously published (numerical) sintering models [31–33], which have also reported that surface diffusion can (indirectly) influence shrinkage rates in this way.

Both surface and grain boundary diffusion reduce the surface area and promote increased inter-splat contact area. However, it is apparent that the reference conditions are such that acceleration of grain boundary diffusion has little effect on the rate of surface area reduction and inter-splat contact area growth, whereas the behaviour is more sensitive to changes in D_{s0} – see Fig. 9(b) and (c). It follows that, if the avoidance of inter-splat bonding is a particular objective, then measures that reduce the rate of surface diffusion are likely to be effective.

5. Conclusions

The following conclusions can be drawn from this work.

(a) A model has been developed for simulation of sintering phenomena in free-standing plasma-sprayed zirconia coatings, based on the variational principle – i.e. microstructural evolution along a path which optimizes the rate of net energy reduction. Its broad validity has been confirmed by comparison with experimental data for shrinkage, surface area, porosity and thermal conductivity.

(b) The model has been used to explore various issues, including the relative sensitivity to pore architecture (microstructure) and material properties, particularly the surface and grain boundary diffusivities.

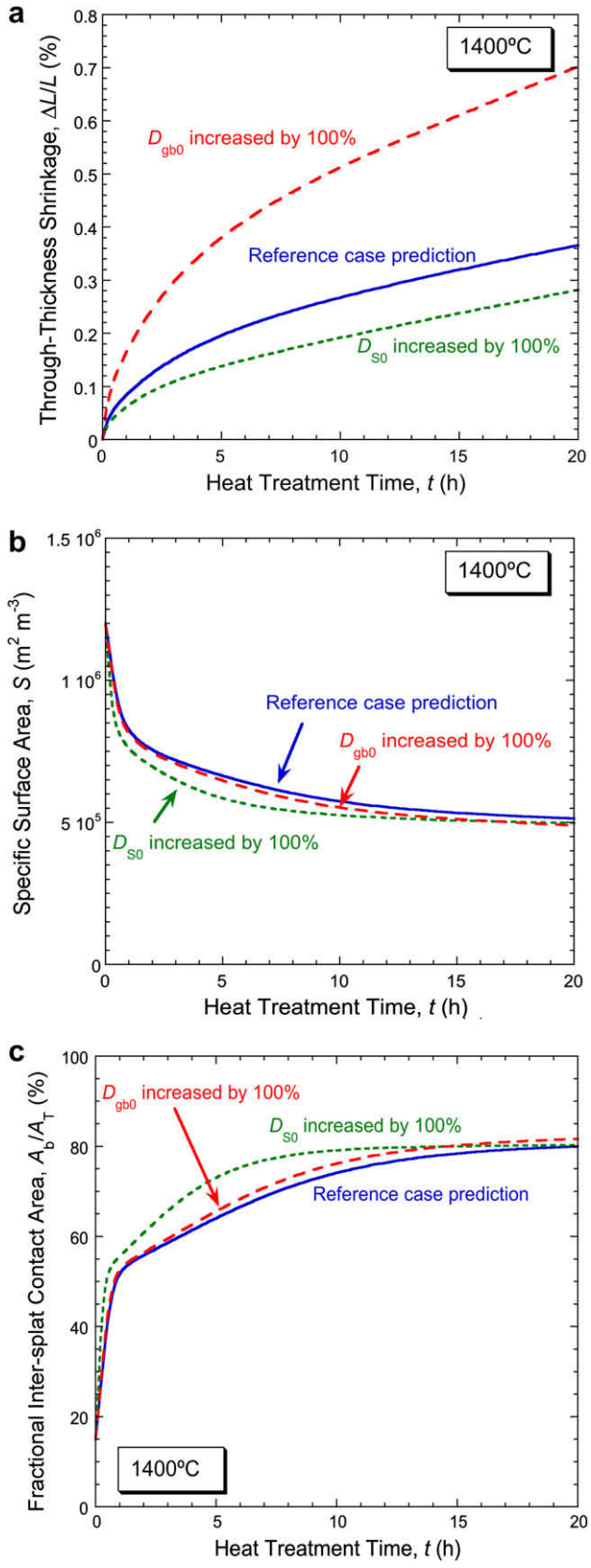

Fig. 9. Predicted sensitivity of (a) through-thickness shrinkage rate, (b) surface area reduction and (c) fractional inter-splat contact area growth, to values of surface and grain boundary diffusivities (pre-exponential constants), for a temperature of 1400 °C and a bimodal distribution of inter-splat pores and microcracks.

(c) As the structure is refined – for example, as the size and spacing of inter-splat contact areas are reduced, or the open pore dimension is decreased – the sintering rate accelerates, as a consequence of the shorter diffusion paths or larger initial curvature gradients, respectively.

(d) Exploration of the effects of input diffusivity values indicates that the model successfully captures the coupling of densifying and non-densifying mechanisms. Predictions indicate that, while surface diffusion does not directly cause any densification, it can indirectly affect shrinkage rates. For example, an increase in the surface diffusivity can reduce shrinkage by quickly consuming the driving force for diffusion (gradients of surface curvature), so that grain boundary diffusion, and the associated densification, is retarded.

(e) The inter-splat contact area affects both the through-thickness thermal conductivity and the in-plane stiffness, and is hence of considerable practical significance. Model predictions indicate that more rapid surface diffusion can accelerate the rate of increase of this contact area, while simultaneously retarding the rate of densification and shrinkage. This highlights the importance of monitoring several experimental indicators of the progression of sintering, which depend on both densifying and non-densifying mechanisms, if the process is to be properly understood and controlled.

(f) Model predictions highlight the sensitivity of the rates of shrinkage and pore spheroidization to both microstructural parameters and (surface and grain boundary) diffusivities. In order to obtain reliable predictions, accurate values are required for both of these sets of parameters.

Acknowledgements

Financial support has come from a Basque Government scholarship (for A.C.), from EPSRC via a Platform Grant (for I.O.G.) and from Sulzer Metco (US) Inc. The authors are grateful for the extensive technical assistance of Sulzer Metco and for various useful discussions with Sulzer Metco personnel, notably Mitch Dorfman and Clive Britton.

Appendix A. Derivation of key equations

A.1. Superposition of domains for a bimodal distribution of pores and microcracks

Assuming superposition of domains corresponding to inter-splat pores, intra-splat microcracks and globular voids, a coating length, L_0, a coating volume, V, and a coating total volume, V_{T0}, which comprises $n^{(1)}_{fine}$ and $n^{(1)}_{coarse}$ inter-lamellar pore domains (open dimension 50 and 200 nm), $n^{(2)}_{fine}$ and $n^{(2)}_{coarse}$ intra-splat microcrack

domains, and $n^{(3)}$ globular void domains, the following relationships can be written:

$$L_0 = n^{(1)}_{\text{fine}} L^{(1)}_{0\_\text{fine}} + n^{(1)}_{\text{coarse}} L^{(1)}_{0\_\text{coarse}} = n^{(2)}_{\text{fine}} L^{(2)}_{0\_\text{fine}} + n^{(2)}_{\text{coarse}} L^{(2)}_{0\_\text{coarse}} = n^{(3)} L^{(3)}_0 \quad \text{(A1)}$$

$$V = n^{(1)}_{\text{fine}} V^{(1)}_{\text{fine}} + n^{(1)}_{\text{coarse}} V^{(1)}_{\text{coarse}} = n^{(2)}_{\text{fine}} V^{(2)}_{\text{fine}} + n^{(2)}_{\text{coarse}} V^{(2)}_{\text{coarse}} = n^{(3)} V^{(3)} \quad \text{(A2)}$$

$$V_{\text{T0}} = n^{(1)}_{\text{fine}} V^{(1)}_{\text{T0\_fine}} + n^{(1)}_{\text{coarse}} V^{(1)}_{\text{T0\_coarse}} = n^{(2)}_{\text{fine}} V^{(2)}_{\text{T0\_fine}} + n^{(2)}_{\text{coarse}} V^{(2)}_{\text{T0\_coarse}} = n^{(3)} V^{(3)}_{\text{T0}} \quad \text{(A3)}$$

The assumption is made that $n^{(1)}_{\text{fine}} = n^{(1)}_{\text{coarse}}$ and $n^{(2)}_{\text{fine}} = n^{(2)}_{\text{coarse}}$.

A.1.1. Coating shrinkage

A net change in length ΔL is given by the sum of the changes from inter-splat pore and microcrack domains

$$\Delta L = n^{(1)}_{\text{fine}} \Delta L^{(1)}_{\text{fine}} + n^{(1)}_{\text{coarse}} \Delta L^{(1)}_{\text{coarse}} + n^{(2)}_{\text{fine}} \Delta L^{(2)}_{\text{fine}} + n^{(2)}_{\text{coarse}} \Delta L^{(2)}_{\text{coarse}} \quad \text{(A4)}$$

Through-thickness and in-plane shrinkage values are given by

$$\left(\frac{\Delta L}{L_0}\right)_{\text{tt}} = -\frac{(h-h_0)_{\text{fine}} + (h-h_0)_{\text{coarse}}}{(h_0)_{\text{fine}} + (h_0)_{\text{coarse}}} \quad \text{(A5)}$$

$$\left(\frac{\Delta L}{L_0}\right)_{\text{ip}} = \left(-\frac{(r_s - r_{s0})_{\text{fine}} + (r_s - r_{s0})_{\text{coarse}}}{(r_{s0})_{\text{fine}} + (r_{s0})_{\text{coarse}}}\right) + \left(-\frac{(a-a_0)_{\text{fine}} + (a-a_0)_{\text{coarse}}}{(a_0)_{\text{fine}} + (a_0)_{\text{coarse}}}\right) \quad \text{(A6)}$$

A.1.2. Surface area

The total surface area is given by Eq. (A7) and the specific surface area by Eq. (A8). The surface area corresponding to intra-splat microcracks is doubled, to account for the two orthogonal arrays of microcracks

$$A_S = (n^{(1)}_{\text{fine}} A^{(1)}_{\text{s\_fine}} + n^{(1)}_{\text{coarse}} A^{(1)}_{\text{s\_coarse}}) + 2(n^{(2)}_{\text{fine}} A^{(2)}_{\text{s\_fine}} + n^{(2)}_{\text{coarse}} A^{(2)}_{\text{s\_coarse}}) + n^{(3)} A^{(3)}_S \quad \text{(A7)}$$

$$S = \frac{A^{(1)}_{\text{s\_fine}} + A^{(1)}_{\text{s\_coarse}}}{V^{(1)}_{\text{fine}} + V^{(1)}_{\text{coarse}}} + 2\frac{A^{(2)}_{\text{s\_fine}} + A^{(2)}_{\text{s\_coarse}}}{V^{(2)}_{\text{fine}} + V^{(2)}_{\text{coarse}}} + \frac{A^{(3)}_S}{V^{(3)}} \quad \text{(A8)}$$

A.1.3. Porosity

The overall porosity is given by

$$P = \frac{(V^{(1)}_T - V^{(1)})_{\text{fine}} + (V^{(1)}_T - V^{(1)})_{\text{coarse}}}{V^{(1)}_{\text{T0\_fine}} + V^{(1)}_{\text{T0\_coarse}}} + 2\frac{(V^{(2)}_T - V^{(2)})_{\text{fine}} + (V^{(2)}_T - V^{(2)})_{\text{coarse}}}{V^{(2)}_{\text{T0\_fine}} + V^{(2)}_{\text{T0\_coarse}}} + \frac{V^{(3)}_T - V^{(3)}}{V^{(3)}_{\text{T0}}} \quad \text{(A9)}$$

The porosity corresponding to intra-splat microcracks is doubled, to account for the two orthogonal arrays of microcracks.

A.2. Free energy of the system

The free energy per unit volume of material is given by

$$G^{(1)}(h, z_s, r_s, N_s) = \frac{1}{V^{(1)}}\left[\gamma_S(\pi(r_s^2 - r_b^2) + 2\pi r_b(h - z_s)). + \gamma_{gb}\left(\frac{1}{2}\pi r_b^2 + \frac{1}{2}\pi r_s^2 + \sqrt{2\sqrt{3}\pi N_s}\frac{1}{r_s}(r_{b0}^2(h_0 - z_{s0}) + r_{s0}^2 z_{s0})\right)\right] \quad \text{(A10)}$$

$$G^{(2)}(a, y_c) = \frac{1}{V^{(2)}}\left[\gamma_S(z_{s0}(L_0 - x_b + a - y_c)) + \gamma_{gb}\left(\frac{1}{2}x_b z_{s0}\right)\right] \quad \text{(A11)}$$

$$G^{(3)} = \frac{\gamma_S(4\pi r_v^2)}{V^{(3)}} \quad \text{(A12)}$$

A.3. Rate of energy dissipation

The rate of energy dissipation per unit volume of material, $\Psi^{(1)}$, corresponding to the interlamellar pore domain, is given by

$$\Psi^{(1)}(\dot{h}, \dot{z}_s, \dot{r}_s, \dot{N}_s) = \Psi^{(1)}_{\text{gb\_z}} + \Psi^{(1)}_{\text{gb\_r}} + \Psi^{(1)}_{\text{s\_r}} + \Psi^{(1)}_{\text{s\_z}} + \Psi^{(1)}_{\text{m}} = \frac{1}{V^{(1)}}\left[\overbrace{\frac{1}{2M_{gb}\Omega\delta_{gb}}\left(\int_{A^{(1)}_{\text{gb\_z}}}(j^{(1)}_{\text{gb\_z}})^2 dA^{(1)}_{\text{gb\_z}} + \int_{A^{(1)}_{\text{gb\_r}}}(j^{(1)}_{\text{gb\_r}})^2 dA^{(1)}_{\text{gb\_r}}\right)}^{\text{Grain boundary diffusion}} + \overbrace{\frac{1}{2M_S\Omega\delta_S}\left(\int_{A^{(1)}_{\text{s\_r}}}(j^{(1)}_{\text{s\_r}})^2 dA^{(1)}_{\text{s\_r}} + \int_{A^{(1)}_{\text{s\_z}}}(j^{(1)}_{\text{s\_z}})^2 dA^{(1)}_{\text{s\_z}}\right)}^{\text{Surface diffusion}} + \overbrace{\frac{1}{2m_m\xi_m}\int_{A^{(1)}_{\text{gb\_z}}}(v^{(1)}_m)^2 dA^{(1)}_{\text{gb\_z}}}^{\text{Grain boundary migration}}\right] \quad \text{(A13)}$$

where the diffusion fluxes and grain boundary migration rate are given by

$$j^{(1)}_{\text{gb\_z}}(z) = -\sqrt{3}(\dot{g})_{\text{gb\_z}} z = -\sqrt{3}\sqrt{\frac{2\pi}{3\sqrt{3}N_s}}\dot{r}_s z \quad \begin{cases} z \in [0,h] \text{if} r \in [0, r_b] \\ z \in [0, z_s] \text{if} r \in [r_b, r_s] \end{cases} \quad \text{(A14)}$$

$$j^{(1)}_{\text{gb\_r}}(r) = -\frac{r}{2}\left(\frac{2h}{r_s}\dot{r}_s + \dot{h}\right) \quad r \in [0, r_b], z = h \quad \text{(A15)}$$

$$j^{(1)}_{\text{s\_r}}(r) = \frac{1}{2}\frac{r_s^2 - r^2}{r}\left(\frac{2z_s}{r_s}\dot{r}_s + \dot{z}_s\right) \quad r \in [r_b, r_s], z = z_s \quad \text{(A16)}$$

$$j^{(1)}_{\text{s\_z}}(z) = \frac{h-z}{h-z_s}\frac{r_s^2 - r_b^2}{2r_b}\left(\dot{z}_s + \frac{2z_s}{r_s}\dot{r}_s\right) + \frac{z_s - z}{h - z_s}\frac{r_b}{2}\left(\dot{h} + \frac{2h}{r_s}\dot{r}_s\right) \quad z \in [z_s, h], r = r_b \quad \text{(A17)}$$

$$v^{(1)}_m = \frac{\sqrt{3}}{2}(\dot{g})_m = -\frac{\sqrt{3}}{2}\sqrt{\frac{\pi}{6\sqrt{3}N_s}}\frac{r_s}{N_s}\dot{N}_s \quad \text{(A18)}$$

The rate of energy dissipation per unit volume of material, $\Psi^{(2)}$, corresponding to the intra-splat microcracks, is given by

$$\Psi^{(2)}(\dot{a},\dot{y}_c) = \Psi^{(2)}_{gb} + \Psi^{(2)}_{S} = \frac{1}{V^{(2)}}\left[\overbrace{\frac{1}{2M_{gb}\Omega\delta_{gb}}\int_{A^{(2)}_{gb}}(j^{(2)}_{gb})^2 dA^{(2)}_{gb}}^{\text{Grain boundary diffusion}} + \overbrace{\frac{1}{2M_{S}\Omega\delta_{S}}\int_{A^{(2)}_{S}}(j^{(2)}_{S})^2 dA^{(2)}_{S}}^{\text{Surface diffusion}}\right] \tag{A19}$$

where the diffusion fluxes are given by

$$j^{(2)}_{gb\_x}(x) = -\dot{a}x \quad x \in [0, x_b] \tag{A20}$$

$$j^{(2)}_{s\_x}(x) = \dot{y}_c(L_0 - x) \quad x \in [x_b, L_0], y = a - y_c \tag{A21}$$

$$j^{(2)}_{s\_y}(y) = -x_b\dot{a} + y\left(\frac{x_b}{a-y_c}\dot{a} + \frac{L_0 - x_b}{a-y_c}\dot{y}_c\right) \quad y \in [0, a-y_c], x = x_b \tag{A22}$$

References

[1] Choules BD, Kokini K, Taylor TA. Surf Coat Technol 1998;106:23.
[2] Singheiser L, Steinbrech R, Quadakkers WJ, Herzog R. Mater High Temp 2001;18:249.
[3] Vassen R, Czech N, Mallener W, Stamm W, Stöver D. Surf Coat Technol 2001;141:135.
[4] Yanar NM, Stiger MJ, Maris-Sida M, Pettit FS, Meier GH. Key Eng Mater 2001;197:145.
[5] Ahrens M, Lampenscherf S, Vassen R, Stöver D. J Therm Spray Technol 2004;13:432.
[6] Lughi V, Tolpygo VK, Clarke DR. Mater Sci Eng 2004;A272:215.
[7] Tsipas SA, Golosnoy IO, Damani R, Clyne TW. Therm. J Spray Technol 2004;13:370.
[8] Rahaman MN, Gross JR, Dutton RE, Wang H. Acta Mater 2006;54:1615.
[9] Mercer C, Faulhaber S, Evans AG, Darolia R. Acta Mater 2005;53:1029.
[10] Kramer S, Yang J, Levi CG, Johnson CA. J Amer Ceram Soc 2006;89:3167.
[11] Chen X. Surf Coat Technol 2006;200:3418.
[12] Strangman T, Raybould D, Jameel A, Baker W. Surf Coat Technol 2007;202:658.
[13] Grant KM, Kramer S, Lof JPAvd, Levi CG. Surf Coat Technol 2007;202:653.
[14] Paul S, Cipitria A, Golosnoy IO, Clyne TW. J Therm Spray Technol 2007;16:798.
[15] Zhu DM, Miller RA. J Therm Spray Technol 2000;9:175.
[16] Renteria AF, Saruhan B. J Europ Ceram Soc 2006;26:2249.
[17] Eaton HE, Novak RC. Surf Coat Technol 1987;32:227.
[18] Siebert S, Funke C, Vassen R, Stöver D. J Mater Proc Technol 1999;93:217.
[19] Thompson JA, Clyne TW. Acta Mater 2001;49:1565.
[20] Choi SR, Zhu DM, Miller RA. J Amer Ceram Soc 2005;88:2859.
[21] McPherson R. Thin Solid Films 1984;112:89.
[22] Golosnoy IO, Tsipas SA, Clyne TW. J Therm Spray Technol 2005;14:205.
[23] Pan J, Cocks ACF, Kucherenko S. Proc R oy Soc Lond A 1997;453:2161.
[24] Cocks ACF, Gill SPA, Pan J. Adv Appl Mech 1999;36:81.
[25] Pan J. Int Mater Rev 2003;48:69.
[26] Hutchinson RG, Fleck NA, Cocks ACF. Acta Mater 2006;54:1297.
[27] Rahaman MN. Ceramic Processing and Sintering. Marcel Dekker; 2003.
[28] Paul S, PhD thesis, University of Cambridge, 2007.
[29] Gustafsson M, Karawacki E, Gustafsson SE. Rev Sci Instrum 1994;65:3856.
[30] Tan JC, Tsipas SA, Golosnoy IO, Paul S, Curran JA, Clyne TW. Surf Coat Technol 2006;201:1414.
[31] Bross P, Exner E. Acta Metall 1979;27:1013.
[32] Exner HE. Acta Metall 1987;35:587.
[33] Svoboda J, Riedel H. Acta Metall Mater 1995;43:1.
[34] Vassen R, Traeger R, Stover D. J Therm Spray Technol 2004;13:396.
[35] McPherson R. Surf Coat Technol 1989;39/40:173.
[36] Allen AJ, Ilavsky J, Long GG, Wallace JS, Berndt CC, Herman H. Acta Mater 2001;49:1661.
[37] Kulkarni A, Gutleber J, Sampath S, Goland A, Lindquist WB, Herman H, et al. Sci Eng A 2004;369:124.
[38] Cipitria A, PhD thesis, University of Cambridge, 2008.
[39] Swaroop S, Kilo M, Argirusis C, Borchardt G, Chokshi AH. Acta Mater 2005;53:4975.
[40] German RN. Sintering Theory and Practice. New York: John Wiley & Sons; 1996.
[41] Kingery WD. J Amer Ceram Soc 1954;37:42.